Electronic Supplementary Information

In operando nanomechanical mapping of PEDOT:PSS thin films in electrolyte solutions with bimodal AFM

Simone Benaglia, Sofia Drakopoulou, Fabio Biscarini, Ricardo Garcia

S1. Bimodal AFM observables

Bimodal AFM nanomechanical reconstruction was applied as already shown in the literature.[1–3] We assumed as mechanical model a Sneddon model for paraboloid tips. Then, the bimodal AFM observables (Figure S1) were translated into nanomechanical properties using the following equations

$$\delta_{max} = \left(\frac{k_1}{2Q_2 k_2}\right)\frac{\left(A_{01}^2 - A_1^2\right)^{1/2}}{\Delta f_2/f_{02}} \qquad \text{S1}$$

$$E_{eff} = \left(\frac{4\sqrt{2}k_1 Q_1}{\sqrt{R}}\right)\left(\frac{k_2}{k_1}\right)^2 \frac{A_1^{3/2}\left(\Delta f_2/f_{02}\right)^2}{A_{01}^2 - A_1^2} \qquad \text{S2}$$

where δ_{max} is the maximum deformation, E_{eff} is the effective Young's modulus ($E_{eff} \approx \dfrac{E_s}{1 - v_s^2}$, where E_s and v_s are the Young's modulus and the Poisson coefficient of the sample), k_1 and k_2 are the spring constants of the first and second mode, Q_1 and Q_2 are the Q-factors of the first and second mode, A_{01} and A_1 are the first mode free amplitude and set-point amplitude, Δf_2 and f_{02} are the second mode frequency shift and resonance frequency, and R is the tip radius. The topography maps shown in the main text were reconstructed by considering the deformation applied to the sample as follows[3]

$$h_{true}(x,y) = h_a(x,y) + \delta_{max}(x,y) \qquad \text{S3}$$

where h_{true} and h_a are respectively the true topography and the apparent topography (output of the first mode).

In dynamic AFM modes, it is possible to convert the AFM observables into the amount of energy dissipated (E_{diss}) by the tip in each oscillation cycle.[4] In our case, we calculated E_{diss} from the first mode observables (amplitude A_{01} and phase ϕ_1)

$$E_{diss} = \frac{\pi k A_1 A_{01}}{Q_1}\left(sin\phi_1 - \frac{A_1}{A_{01}}\right) \qquad \text{S4}$$
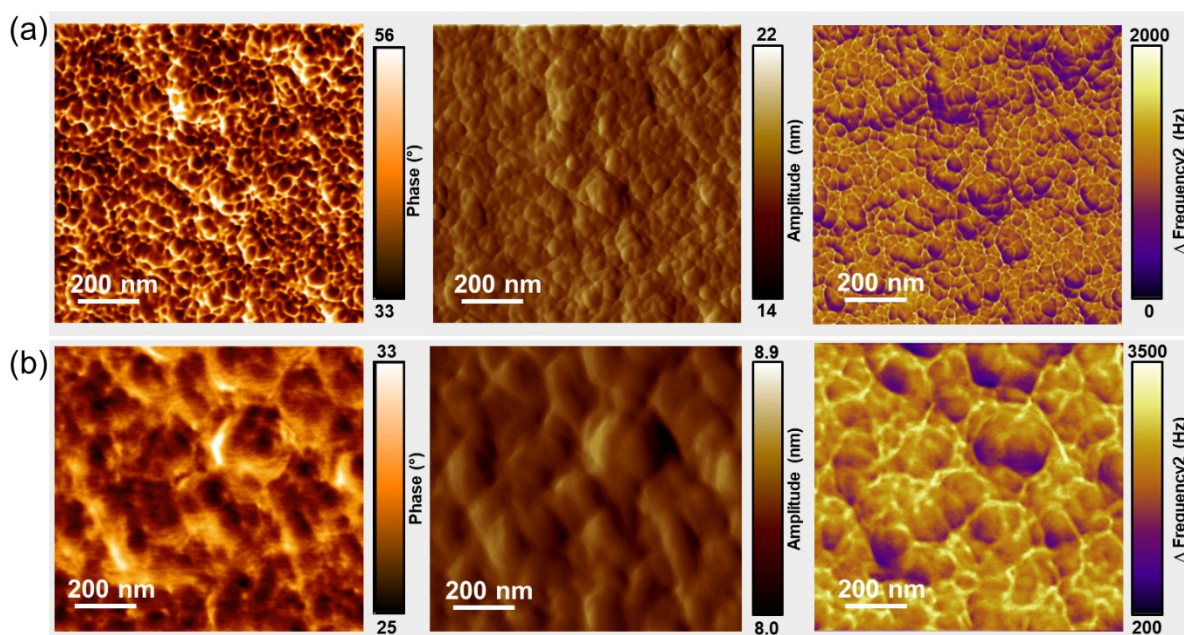
Figure S1. Bimodal AFM observables in air and aqueous solution on PEDOT:PSS. First mode phase and amplitude and second mode frequency maps of PEDOT:PSS in air (a) and in liquid solution (b). The images correspond to the bimodal AFM maps shown in Figure 2.
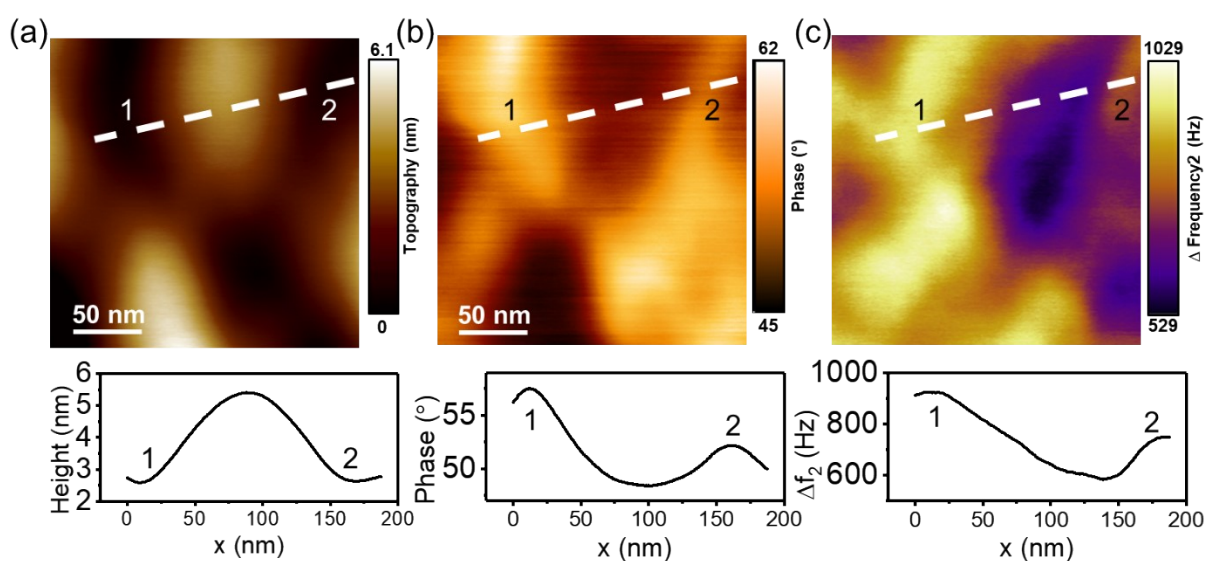

Figure S2. (a) Maps of bimodal AFM topography, (b) 1st mode phase shift, and (c) 2nd mode frequency shift. Corresponding cross sections taken along the white dotted lines are shown below. Region 1 and 2 are "valleys" with the same height though they have a different phase and frequency shift. The higher phase shift value of the PSS regions is not induced by a particular morphology.

S2. Capillary force probed by Force Curves

We performed AFM force curves (FCs) to determine what was the contribution to the dissipative forces probed in bimodal AFM. Figure S3 shows two typical FCs obtained on low and high energy dissipation regions (PEDOT-rich cores and PSS matrix). The energy that is dissipated due to non-conservative capillary forces is represented by the grey area in between the approaching and retracting curve ($E_{\text{diss-cap}}$).[5] The regions associated with the PSS matrix presented an average $E_{\text{diss-cap}} = 137.3 \pm 16.3$ eV, while the ones linked to PEDOT-rich cores showed an average $E_{\text{diss-cap}} = 80.6 \pm 17.7$ eV. These results highlight the strong hydrophilic nature of PSS shell and matrix: in fact, the presence of PSS-rich areas strongly attracts water molecules from the air, that in turns interact with the AFM tip with strong capillary forces.
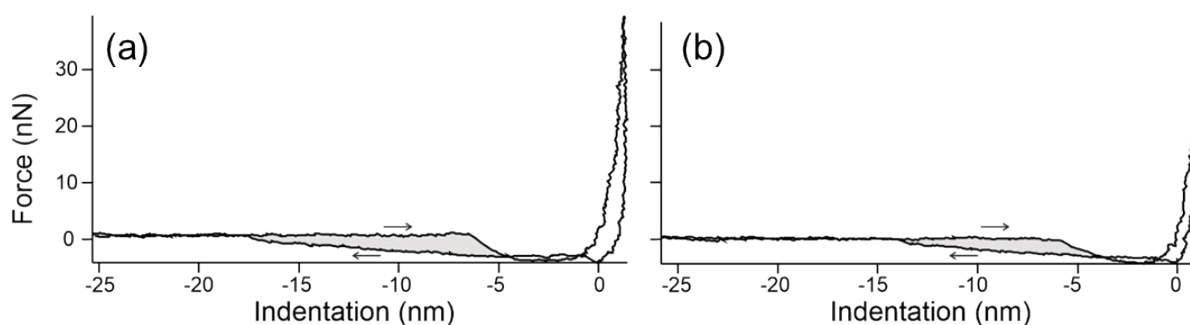

Figure S3. Force curves (FCs) on PEDOT:PSS. FCs realized on (a) PSS-rich areas and on (b) PEDOT-rich cores. The approaching and retracting curves are identified by the direction of the arrows. The grey area in between the two curves is the consequence of dissipative capillary interactions. The grey area of the curve in (a) is greater than the one in (b). This highlights how the regions rich in PSS have a stronger hydrophilic character, with sulfonate groups free to form hydrogen bonds with water molecules.

S3. Electrical stage set-up

A home-made electrical set-up was implemented on top of the AFM holder of a Cypher S (Asylum Research, Oxford Instruments, Ca, USA). Figure S4 shows the AFM stage, the Pt electrode, and the electrical connections. Voltage bias was applied between the Pt electrode and the gold electrode below the PEDOT:PSS film (ΔV vs V_{OC}). The ion injection could be monitored directly through the internal optics of the AFM. In fact, upon application of $\Delta V = 0.8$ V, the polymer is reduced and changes its color (electrochromic switch).[6]
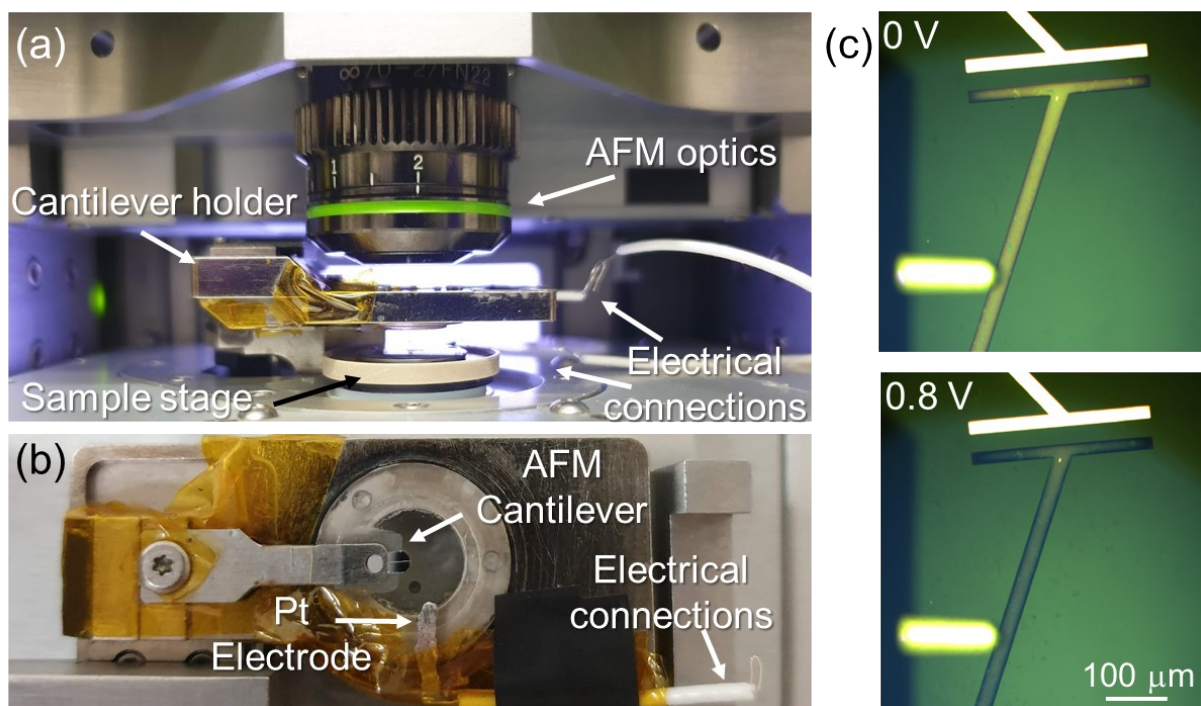
Figure S4. Electrical stage for bimodal AFM measurements. (a) The AFM holder of a Cypher AFM was modified by adding a flat Pt electrode at the cantilever side; this was connected through a thin wire to the SMU. (b) Bottom view of the AFM set-up and electric stage. (c) The electrochromic response of the PEDOT:PSS film was recorded with the internal optics of the Cypher AFM. Due to the application of a reduction potential ($\Delta V = 0.8$ V), the polymer changes color.

S4. Bimodal AFM experiments

Bimodal AFM experiments addressed how the mechanical properties of PEDOT:PSS changed due to the uptake of ions from the electrolyte solution. We performed three sets of experiments: (i) $\Delta V = 0/0.8$ V, (ii) $\Delta V = V_{OC}$, and (iii) $\Delta V = 0/-0.5$ V. Figure S5 shows an experiment where cycles of $\Delta V = 0/0.8$ V were applied, in a similar way to the one in Figure 6a. Our results clearly demonstrate that the mechanical properties of the polymer film change only by cations injection.
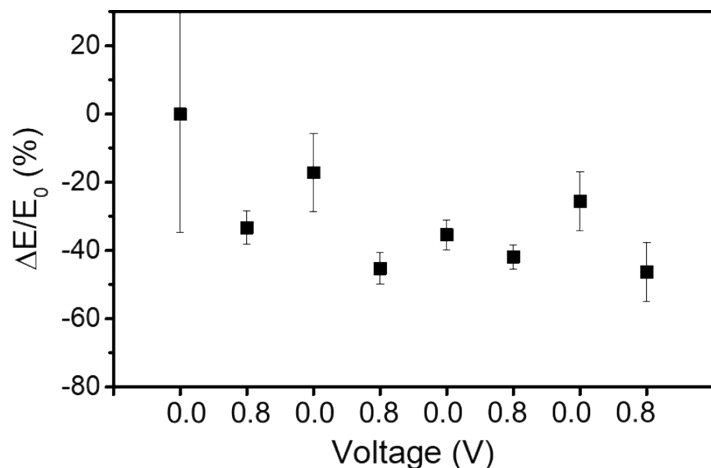
Figure S5. Dependence of PEDOT:PSS elastic properties on the applied voltage. The relative change of elastic modulus $\Delta E = (E_i - E_0)/E_0$, where E_i is the modulus probed at each voltage, and E_0 is the modulus recorded at the beginning of the experiment. The application of a positive voltage at the top electrode ($\Delta V = 0.8$ V) forces cations inside the PEDOT:PSS film and its Young's modulus drops. When the de-doping voltage is removed by re-applying 0 V, ions outflow from PEDOT:PSS to the solution.

S5. Molecular resolution images of PEDOT:PSS

We were not able to obtain molecular resolution images, where the lamellar structure of the polymer is resolved, by standard AFM topography. To obtain high-spatial resolution images (sub-1 nm) we implemented an AM feedback on the 2nd eigenmode of the cantilever. In addition, we used very small amplitudes (≤0.3 nm). This is a multifrequency AFM approach that was successfully applied to generate atomic-scale images of solid-liquid interfaces[7] and to provide molecular resolution images crystalline and polymer surfaces.[8,9]

The molecular resolution images revealed two distinct periodic patterns characterized, respectively, by 0.79 nm (Figure S6a) and 1.25 nm (Figure S6b) pitch. The above values are consistent with the values obtained by X-ray diffraction measurements.[10] These values enable us to ascribe the smaller periodicity to the ordering of PSS chains while the largest periodicity corresponds to the lamellar structure of PEDOT molecules.
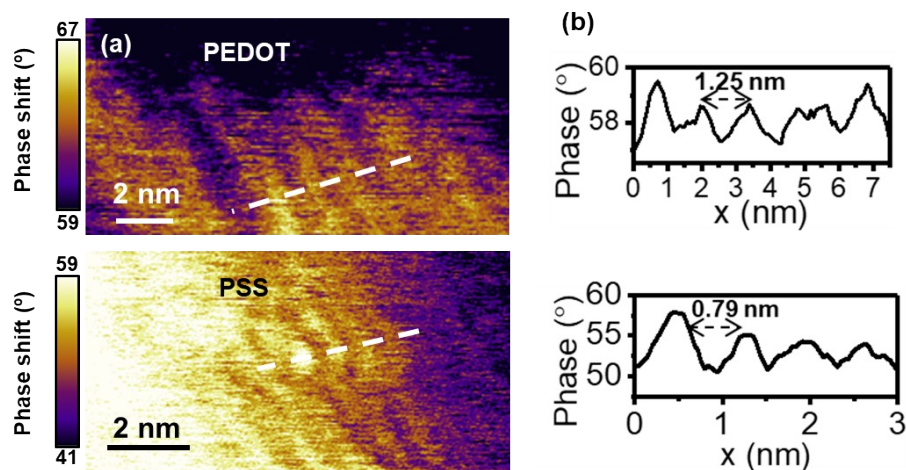
Figure S6. (a) Molecular chain resolution AFM phase images of PEDOT (top) and PSS (bottom) domains in a PEDOT:PSS film; 190 x 97 pixels. (b) Cross-sections along the lines marked in (a). Imaging values were, $A_{02} = 0.45$ nm, $A_2 = 0.25$ nm, the scanning frequency in the fast direction was of 8.7 Hz for the PEDOT and 11.2 Hz for PSS.

Table S1.

Figure	Cantilever	medium	k_1 (N/m)	Q_1	f_1 (kHz)	A_{01} (nm)	A_1 (nm)	k_2 (N/m)	f_2 (kHz)	A_2 (nm)	R (nm)
2	PPP-NCHAuD	air	46.0	589.9	346.6	33.0	18.0	2376.0	2135.0	0.8	15
3a	PPP-NCHAuD	air	46.0	589.9	346.6	33.0	18.0	2376.0	2135.0	0.8	15
3b	HQ-150-AuD	50mM KCl	11.6	6.7	90.7	16	7.0	560.0	609.3	0.2	13
4, 6	HQ-150-AuD	50mM KCl	5.9	5.9	69.4	16	9.8	224.7	464.4	0.2	
S5	PPP-NCSTAuD	50mM KCl	9.9	5.3	55.6	11	5.7	418.4	379.19	0.2	

References

1   C. A. Amo, A. P. Perrino, A. F. Payam and R. Garcia, *ACS Nano*, 2017, **11**, 8650–8659.

2   S. Benaglia, V. G. Gisbert, A. P. Perrino, C. A. Amo and R. Garcia, *Nat. Protoc.*, 2018, **13**, 2890–2907.

3   S. Benaglia, C. A. Amo and R. Garcia, *Nanoscale*, 2019, **11**, 15289–15297.

4   T. R. Rodriguez and R. Garcia, *Appl. Phys. Lett.*, 2004, **84**, 449–451.

5   V. Barcons, A. Verdaguer, J. Font, M. Chiesa and S. Santos, *J. Phys. Chem. C*, 2012, **116**, 7757–7766.

6   E. Stavrinidou, P. Leleux, H. Rajaona, D. Khodagholy, J. Rivnay, M. Lindau, S. Sanaur and G. G. Malliaras, *Adv. Mater.*, 2013, **25**, 4488–4493.

7   D. Martin-Jimenez, E. Chacon, P. Tarazona and R. Garcia, *Nat. Commun.*, 2016, **7**, 12164.

8   T. Fukuma, K. Kobayashi, K. Matsushige and H. Yamada, *Appl. Phys. Lett.*, 2005, **87**, 034101.

9   V. V. Korolkov, A. Summerfield, A. Murphy, D. B. Amabilino, K. Watanabe, T. Taniguchi and P. H. Beton, *Nat. Commun.*, 2019, **10**, 1–8.

10   E. Hosseini, V. Ozhukil Kollath and K. Karan, *J. Mater. Chem. C*, 2020, **8**, 3982–3990.